A dynamical approach to precision entry in multi-body regimes: Dispersion manifolds

B.G. Marchand [a,b,*], S.K. Scarritt [c], T.A. Pavlak [a], K.C. Howell [a]

[a] Purdue University, 701 W. Stadium Ave., West Lafayette, IN 47907, United States
[b] Decisive Analytics Corporation, 1235 South Clark Str., Ste. 400, Arlington, VA 22202, United States
[c] The University of Texas at Austin, 210 E. 24th St, Austin, TX 78712, United States

ARTICLE INFO

ABSTRACT

The identification of trajectories that target a precise location and approach vector during planetary entry is sensitive to the quality of the startup arc supplied to iterative path planning and guidance algorithms. These sensitivities are especially evident when multi-body effects are significant; low-energy spacecraft trajectories that dwell near the gravitational boundary of two bodies, for instance, are more susceptible to third-body effects. Dynamical sensitivities are also significant when maneuvers are scheduled within a region of space susceptible to multi-body effects. The present study considers precision entry targeting from the perspective of the multi-body problem.

© 2013 IAA. Published by Elsevier Ltd. All rights reserved.

1. Introduction

Precision entry targeting, in this study, refers to the identification of all maneuvers necessary to guide the vehicle to a specific location on a rotating body with a pre-specified approach vector at entry interface. In the present study, precision entry targeting is considered in the context of the perturbed restricted three body problem. The primary bodies under consideration are the Earth and the Moon and the problem is defined as "restricted" because the mass of the spacecraft is assumed to be significantly smaller than that of the primaries. Furthermore, "perturbed" suggests that the motion of the primary bodies is consistent with an ephemeris model; that is, the position and velocity of the primaries are derived from planetary ephemerides. In the perturbed restricted three-body problem, targeting processes (optimal or suboptimal) are sensitive to the quality of the startup solution provided. Generally speaking, gradient based targeting algorithms, whether optimal or suboptimal, are not self-starting and thus depend on the availability of a reasonably accurate initial guess (i.e. startup solution). Since the dynamical model is not time invariant, the success of any targeting process can be sensitive to both the temporal and spatial scheduling of deterministic maneuvers along the path.

Startup arcs employed in iterative path planning and guidance algorithms often rely on conic or patched-conic approximations for the identification of startup solutions. Of course, two-body approximations are not always sufficiently accurate for trajectory design in multi-body regimes. This is particularly true when the path of the vehicle is expected to escape the Hill sphere with a relatively low energy level. As the vehicle transitions through a dynamically sensitive region, the gravitational influence of the primaries and the perturbing bodies can

---

* Corresponding author at: Decisive Analytics Corporation, 1235 South Clark Str., Ste. 400, Arlington, VA 22202, United States. Tel.: +1 512 627 4785; fax: +1 512 233 2349.

E-mail address: belinda.marchand@dac.us (B.G. Marchand).

introduce significant deviations from the intended path. This, in turn, affects the efficiency of iterative path planning and guidance algorithms that seek to fine tune the transfer parameters to achieve a precise set of entry conditions at a specific body within a multi-body system. It also affects the subset of phase space explored by the algorithms in attempting to identify a feasible transfer.

The manifestation of these dynamical sensitivities is easily observed in the three-maneuver trans-Earth injection (TEI) sequence originally envisioned to transfer the Orion vehicle from low lunar polar orbit to a specified Earth arrival condition [1]. The initial design of this sequence, rooted in two-body analysis, is illustrated in Fig. 1(a) and the associated maneuver schedule is shown in Fig. 1(b). The first maneuver (TEI-1), in Fig. 1, seeks to raise the apoapsis of the initial lunar orbit. The second maneuver (TEI-2) executes a change in orbital inclination. The third and final maneuver (TEI-3) injects the spacecraft into its final return path.

The present investigation offers some preliminary insight into the precision entry problem in multi-body regimes. Initially, this is accomplished by generating an ensemble of dispersion trajectories associated with a representative set of possible entry interface states relative to the rotating target body. This ensemble of dispersion trajectories represent a subset of a "manifold" surface associated with a particular entry interface state. That is, this surface represents the subset of the dynamical flow that converges onto the vicinity of the specified entry state. The perturbed restricted three-body problem serves as the initial framework for this analysis. A fundamental understanding for the interaction between the dispersion manifolds and the Hill sphere is sought. The goal is to assess entry constraint coupling and sensitivities which may affect the process by which startup arcs, for targeting, guidance, and optimization processes, are subsequently identified.

2. Background

The Hill sphere is defined in the synodic rotating frame of the circular restricted three-body problem (CR3BP) [2]. In this frame, it is assumed that the primaries evolve along circular orbits about their common center of mass. The rotating x-axis is directed from the larger to the smaller primary such that both remain equidistant along that line for all time. The z-axis is normal to the plane of their orbits while the y-axis completes the right-handed triad. The Hill sphere itself is centered at the smaller of the two primary bodies. In the Earth–Moon system, the radius of the sphere (r_s) is approximately determined as [3]

$$r_s = a \sqrt[3]{\frac{\mu_{Moon}}{3\mu_{Earth}}}. \tag{1}$$

where μ_{Earth} and μ_{Moon} represent the gravitational parameters for the Earth and Moon, respectively, and a is the semi-major axis of the Moon's orbit around the Earth. In this system, the relative size of the Hill sphere, in relation to the Earth, Moon, and the libration points of the CR3BP, is illustrated in Fig. 2.

Since the Hill sphere is defined in the CR3BP, where the primary bodies remain equidistant for all time, identifying an equivalent Hill sphere in the general perturbed three-body problem requires that all trajectories be transformed into a properly scaled set of coordinates. For instance, if the Earth–Moon dynamics are derived from ephemeris information, the inertial (I) position and velocity vectors of the Moon, with respect to the Earth, in terms of inertial coordinates are given by $\boldsymbol{r}_I^{EM}$ and $^I\boldsymbol{v}_I^{EM}$, respectively. These vectors are then used to define an instantaneous synodic rotating frame (R) in terms of unit vectors $\hat{r}_1$, $\hat{r}_2$, and $\hat{r}_3$ where

$$\hat{r}_1 = \frac{\boldsymbol{r}_I^{EM}}{\|\boldsymbol{r}_I^{EM}\|}, \tag{2}$$
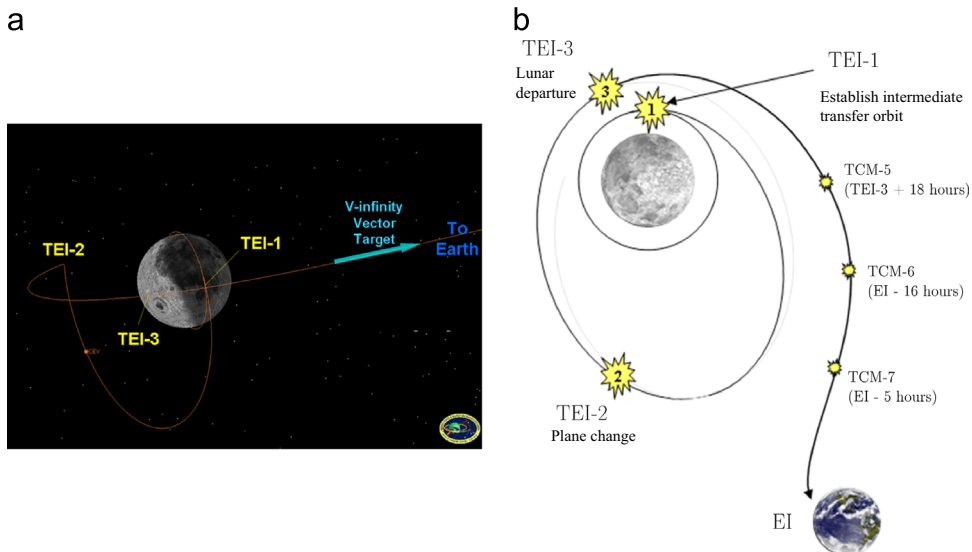
a

b

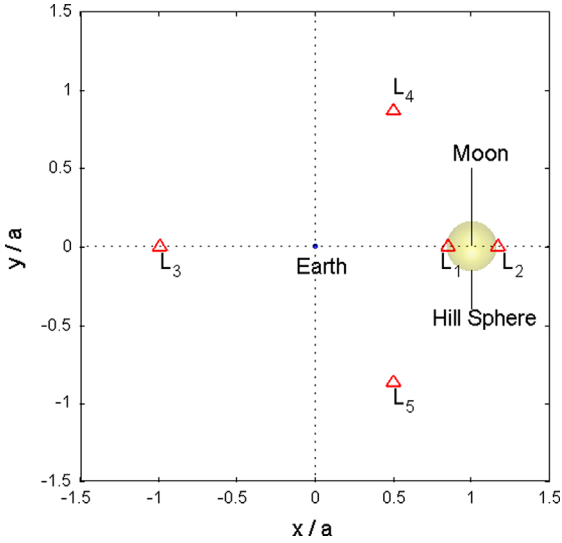**Fig. 1.** Orion trans-Earth trajectory and maneuver schedule. (a) Return trajectory. (b) Maneuver schedule.

Fig. 2. CR3BP Hill sphere: Earth centered synodic frame.

$$\hat{r}_3 = \frac{\boldsymbol{r}_I^{EM} \times {}^I\boldsymbol{v}_I^{EM}}{\|\boldsymbol{r}_I^{EM} \times {}^I\boldsymbol{v}_I^{EM}\|}, \tag{3}$$

$$\hat{r}_2 = \hat{r}_3 \times \hat{r}_1. \tag{4}$$

Subsequently, if the spacecraft (S) inertial state is described by $\boldsymbol{r}_I^{ES}$ and ${}^I\boldsymbol{v}_I^{ES}$, a state transformation is implemented such that $\boldsymbol{r}_I^{ES} \rightarrow \boldsymbol{r}_R^{ES}$ and ${}^I\boldsymbol{v}_I^{ES} \rightarrow {}^R\boldsymbol{v}_R^{ES}$. The resulting state vector is non-dimensionalized by the instantaneous distance between the primaries and the instantaneous mean motion as determined from the available ephemerides.

In this instantaneous synodic frame, and in terms of this new set of scaled coordinates, the intersection of each transformed dispersion manifold with the Hill sphere is represented as a locus of points. The collection of all dispersion loci for a given Earth entry interface (EEI) state is useful, for instance, in identifying whether a departure strategy for one EEI state is also suitable for others. The loci are also useful in designing alternate departure schemes, specifically those that consider the use of non-conic arcs derived from multi-body analysis. The understanding gained from the study of the dispersion loci allows the designer to determine whether or not a conic departure strategy is likely to succeed, how it could be modified, or whether an alternate departure strategy is necessary. Furthermore, designing startup arcs in terms of non-dimensional synodic coordinates is ultimately convenient since the position of the primary bodies is fixed in this frame.

Improved startup arcs promote computational efficiency in gradient-based iterative targeting [4,1,5] and optimization [6–11] algorithms. That is because gradient-based algorithms search for solutions in the immediate neighborhood of the startup arc. As a result, the solutions identified often resemble the startup arc in many ways. This excludes, however, many other types of solutions that may offer improved trajectory options. Thus,

developing a better understanding of the dynamical flow associated with the types of solutions sought is an important initial step in any targeting or optimization process.

A dynamical systems approach often proves essential in acquiring this understanding in multi-body regimes [12–14]. In this case, the phase space structure is characterized in terms of stable, unstable, and center manifold flows around specific types of reference solutions. In this study, we draw an analogous interpretation to define sets of dispersion manifolds and analyze the sensitivities associated with specific EEI parameters. The general intent is to understand and exploit the dynamical structure of the Earth–Moon system to identify feasible and lower cost startup arcs that more closely satisfy the precision entry goals and mission criteria a priori. No restrictions are placed on the geometry of the solutions or the location of the maneuvers.

The example of application selected in this study is centered around the Orion trans-Earth injection [1]. Thus, at most, five entry parameters are targeted: altitude (h), flight path angle (γ), geocentric latitude (ϕ) and longitude (λ), and flight path azimuth (χ) [1]. The altitude, latitude, and longitude determine the position components of the EEI state. The flight path angle and azimuth, then, characterize the approach vector for the incoming velocity. The entry speed itself is not constrained, nor is the entry time. However, for the purpose of constructing the dispersion manifolds, a representative entry speed and time are selected based on previous studies [1] and held fixed. Then, one at a time, perturbations are applied over a designated range to each of the remaining entry parameters relative to its nominal value while the other parameters are held fixed. The resulting ECI state vector associated with these EEI conditions is referred to as the "perturbed" state.

The spacecraft state at EEI is defined in the Earth Mean Equator and Equinox of J2000 (EMEJ2000) frame. This is consistent with the reference frame employed in the JPL DE405 ephemerides [15]. Subsequently, these inertial perturbed states are numerically integrated backwards in time in the ephemeris model until the trajectory intersects the Hill sphere. The ephemeris model, in this case, assumes that the Sun, Earth, and Moon states are available directly from the DE405 ephemerides [15]. Thus, only the spacecraft state is numerically integrated while the states of the primaries and perturbing bodies (e.g. the Sun) are assumed to be known functions of time. The trajectories associated with one of the five entry parameters are used to construct the dispersion manifold for that quantity.

For each EEI state, then, a total of five dispersion manifolds are generated. The associated trajectories are transformed into the synodic rotating frame of the Earth–Moon system [2] and non-dimensionalized. The loci of intersections of the dispersion manifolds with the Hill sphere, defined in this scaled synodic frame, are identified. Then, the significance of the intersection loci, and their impacts on lunar departure strategies, is addressed.

To illustrate the impact of third and fourth body effects on the return strategy, a series of sample returns are

considered next. At first, the examples are focused on an emergency contingency case: targeting only altitude and flight path angle. A targeting algorithm [1] is applied on a reasonable yet infeasible solution so that the entry altitude and flight path angle are met without violating the available fuel budget. However, as previously mentioned, the quality of that startup arc limits the neighborhood that targeting and gradient-based optimization algorithms explore. Thus, a simple numerical continuation scheme is applied on the resulting arcs to explore the available solution space further and lower the transfer costs. Continuation, in this case, refers to the process of perturbing a previously converged solution and re-converging under a new set of constraints in the neighborhood of the initial constraint set considered previously. Significant cost reductions are achieved as a result. The newly converged solutions are employed in a targeting algorithm [1] to assess the sensitivity of the entry parameters relative to the startup solution.

3. Dispersion analysis example: applications to Orion trans-Earth injection

Earlier studies obtain startup arcs for the three-maneuver return sequence by dividing the design process into two parts [16]. First, the lunar return segment is designed, in a Moon centered inertial (MCI) frame, using conic arcs. Specifically, the spacecraft in low lunar orbit performs a maneuver to raise apoapsis, then a second maneuver to change the inclination of the plane, and a third maneuver to raise the energy enough to escape the vicinity of the Moon in the general direction of the Earth. These maneuvers, planned in the two-body problem, are then implemented in the ephemeris model of the lunar segment. Of course, the resulting path – in the ephemeris model – does not resemble the two-body solution due to the impact of third body effects on this particular type of return sequence. The second part of the process first requires that a partial EEI constraint be specified and translated into a full state vector by assuming values for the unspecified quantities, in this case entry speed. Then, this state is propagated backwards in time until the trajectory crosses a user specified interface region [16]. The results are then used in some user-selected targeting process, typically an optimization routine, that seeks to bridge the gap at the interface region and also meet the remaining constraints along the path. One drawback of this approach is that the startup arcs obtained from this two-body approximation can exhibit large spatial and temporal discontinuities at the interface region. This can have a negative impact on the numerical efficiency of any

targeting or optimization algorithm that only explores the vicinity of the startup arc for feasible or optimal solutions. It is also true that even if the discontinuity is not unreasonable at the interface region, the entry state was not fully specified during the backward propagation of the Earth segment. Thus, either feasible or optimal targeting algorithms would have to both bridge the spatial and temporal gap at the interface region and potentially correct very large errors in the entry state.

Precision entry, in this case, requires that the vehicle achieves specific altitude, flight path angle, flight path azimuth, and geocentric latitude and longitude at Earth entry. Of these quantities, the geocentric longitude and the flight path azimuth are both measured in coordinate frames that are fixed on the rotating Earth. Thus, the entry time becomes a critical factor in determining whether or not the entry state is met.

Six sample Earth entry interface (EEI) sites are considered [17–20]. The corresponding EEI state parameters are associated with an altitude (h) of 121.912313 km, and an entry speed (V) of 10.992728 km/s. Subsequently, each EEI state is uniquely determined by their geocentric latitude (ϕ), longitude (λ), the flight path angle (γ), and flight path azimuth (χ) as defined in Table 1.

The inertial entry state, determined from these parameters, is integrated backwards in time until it intersects the Hill sphere around the Moon. If the trajectory does not cross the Hill sphere, the integration is terminated after a time-of-flight of five days [20]. This first arc defines the "nominal" path to the entry site specified. To generate the dispersion manifold, then, the "nominal" path, at the specified epoch time, is systematically perturbed. That is, a small variation is applied to one of the five entry parameters: altitude, latitude, longitude, flight path angle, and flight path azimuth. This causes a perturbation of the initial ECI state to be integrated. While holding the speed, the entry time, and all four remaining parameters fixed, the ECI states associated with a specific set of perturbations are propagated backwards in time to generate the associated dispersion manifold. Once again, the integration process stops when either the Hill sphere is reached or the reference time of flight is exceeded.

Once the dispersion manifolds are generated, the next step is to determine whether or not the associated trajectories intersect the Hill sphere, selected here to define the lunar "interface" region. This is accomplished by transforming the dispersion manifolds into Earth–Moon non-dimensional synodic coordinates and numerically searching for intersections with the Hill sphere. Naturally, whether or not intersections exist is largely dependent on the time associated with the Earth entry

Table 1
Entry interface parameters.

Parameter	EEI-1 (deg)	EEI-2 (deg)	EEI-3 (deg)	EEI-4 (deg)	EEI-5 (deg)	EEI-6 (deg)
λ	−115.5	−121.00	−134.5456	−151.4038	173.5216	175.6365
ϕ	−46.66992	−8.8522	−19.20410	−7.14720	15.36700	15.36700
χ	0.0	0.0	13.9960	34.1065	62.3311	49.3291
γ	−5.81	−5.99	−6.03	−6.16	−6.16	−5.86

interface state, which is the initial time of the integration. If the reference entry time for a particular nominal trajectory (with all entry parameters unperturbed) does not lead to an intersection, this entry time is adjusted manually, via increments of approximately 3 h, until the trajectory intersects the Hill sphere. Future studies will investigate the development of a timing condition for determining appropriate entry times for trajectories in the Earth–Moon system.

To visualize the geometry of the intersections, the Hill sphere is divided into a standard grid of latitude and longitude. Here, longitude is measured along the Earth–Moon orbital plane, relative to the instantaneous Earth–Moon line, which is denoted as 0° longitude in Fig. 3(a)–(f). If the intersection occurs above the Earth–Moon plane, the latitude of the intersection along the sphere is defined as positive. Fig. 3(a)–(f) each illustrates five loci of points, which represent the intersections of a specific dispersion manifold with the sphere.

For each dispersion manifold, the range of perturbations that lead to trajectories that intersect the Hill sphere is summarized in Table 2. The maximum allowable perturbation range, chosen heuristically, is ±10° for the angle quantities and ±100 km for altitude. Perturbations outside the ranges listed in Table 2, however, do not intersect the Hill sphere. In relation to this data, the arrows listed in the legend for Fig. 3(a)–(f) indicate the direction of motion along the loci, from the minimum to the maximum values listed in Table 2. The direction of the flow along the loci is crucial to our understanding of constraint coupling, discussed later in this document.

The latitude and flight path angle loci in Fig. 3(a)–(f) exhibit the largest spread along the Hill sphere. However, of the angular quantities targeted, the data in Table 2 suggests that the flight path angle dispersion manifolds exhibit the least number of intersections with the Hill sphere. Thus, while the dispersion curve on the sphere appears wide, it is associated with a much smaller range of errors relative to the desired nominal value. This suggests small changes in flight path angle at entry have a significant effect on the overall geometry of the transfer arc near the Moon. Furthermore, although the altitude dispersion spread on the sphere does not appear as significant as flight path angle, many of the altitudes selected did not lead to intersections with the sphere. Of course, given that the entry speed is fixed, this is not surprising since the only parameter targeted that affects orbital energy is the altitude at entry.

Intersections of the dispersion manifolds with the Hill sphere, and how widely the locus of intersections spreads
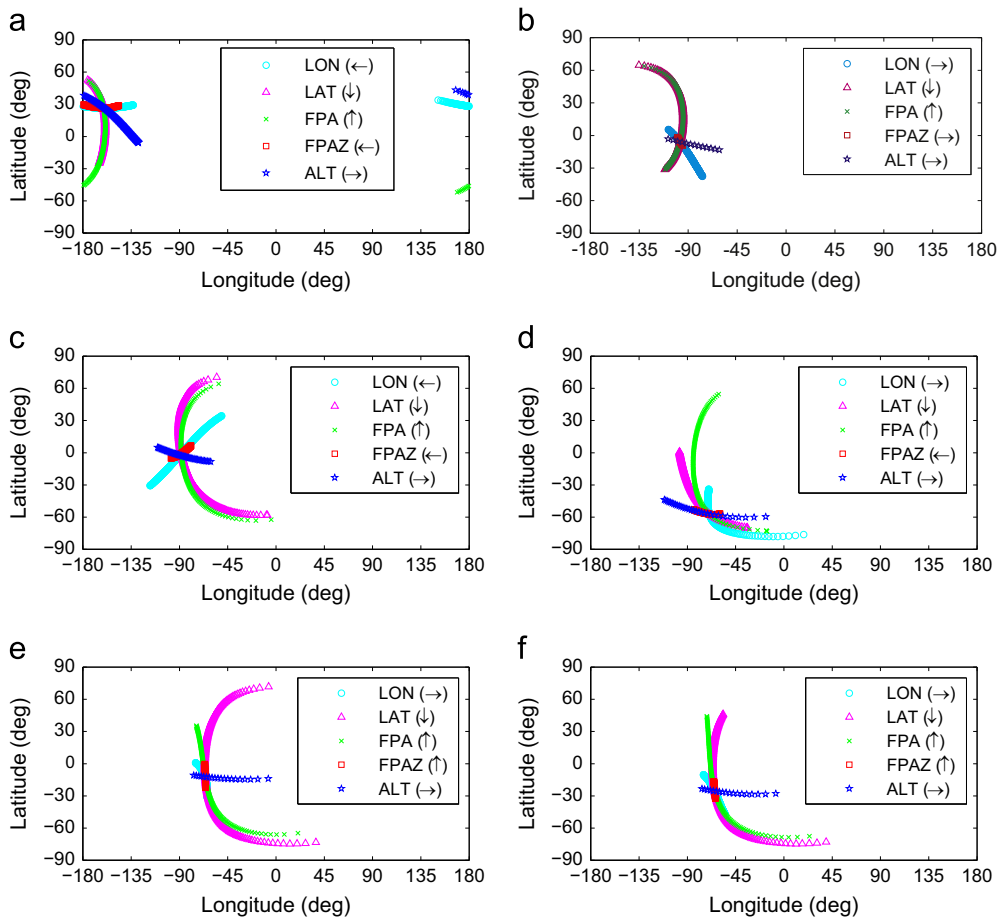

Fig. 3. Intersections of EEI dispersion manifolds with Hill sphere. (a) EEI-1. (b) EEI-2. (c) EEI-3. (d) EEI-4. (e) EEI-5. (f) EEI-6.

Table 2
EEI range of initial perturbations that lead to intersections with Hill sphere.

EEI	h (km)		ϕ (deg)		λ (deg)		γ (deg)		χ (deg)	
	Min.	Max.	Min.	Max.	Min.	Max.	Min.	Max.	Min.	Max.
1	−11.28	95.99	−2.93	10.00	−7.79	7.24	−7.34	1.43	−10.00	10.00
2	−1.25	4.76	−10.00	4.99	−3.63	10.00	−2.43	4.89	−10.00	10.00
3	−7.27	17.79	−8.85	9.95	−8.85	10.00	−4.69	3.73	−10.00	10.00
4	−30.83	4.76	−10.00	1.73	−6.29	4.34	−0.93	7.39	−10.00	10.00
5	−2.26	7.27	−9.95	8.05	−10.00	10.00	−5.69	5.34	−10.00	10.00
6	−2.26	6.27	−10.00	6.29	−10.00	10.00	−3.43	5.84	−10.00	10.00

along the surface of the sphere itself, both introduce two distinct issues that impact the design process. If, for instance, a two-body conic analysis is employed in selecting startup arcs, it is important that the dispersion manifolds for the desired EEI states intersect with the sphere in an orientation that facilitates the construction of a lunar departure arc to interface with the Earth segment of the trajectory. A startup arc with large state and/or temporal discontinuities at the interface region can have a detrimental effect on the computational efficiency of any targeting process. Large discontinuities at the interface state can also influence the subset of phase space that a targeting or optimization algorithm searches. This, in turn, can have a negative effect on the cost of merging the Earth and Moon segments and transitioning them into a single feasible transfer trajectory.

Of course, a wide range of dispersions on the Hill sphere is not, in itself, an undesirable feature. In fact, a wide dispersion on the Hill sphere may be indicative of increased flexibility regarding the quality of the startup arc. For instance, a startup arc that exhibits significant errors in that entry parameter may still qualify as a reasonable initial guess because properly scheduled maneuvers can identify neighboring trajectories that both (a) originate from the Moon and (b) are closer to the desired EEI state. This is demonstrated in the last section of this paper with the longitude and latitude constraints.

The flight path azimuth dispersions, in contrast, intersect the Hill sphere for all six EEI states considered. That is, the entry flight path azimuth may be off by up to $\pm 10°$, and the associated entry manifolds will still intersect the Hill sphere near the same region. However, Fig. 3(a)–(f) indicates that these intersections occur in a very narrow and confined region of the sphere, unlike the latitude and flight path angle dispersions which span a significant spread along the sphere. Thus, designing a lunar transfer, for precision entry, essentially requires that the lunar segment target a very precise neighborhood of the Hill sphere. For instance, let N_a denote the subset of the dispersions on the Hill sphere that correspond to the errors in azimuth and N_l denote the subset of the dispersions that correspond to errors in latitude. The neighborhood defined by N_a is smaller, in this case, than that defined by N_l. In designing the lunar segment of the trajectory, one seeks startup arcs that exist in the region defined by $N_a \cap N_l$. Of course, this neighborhood only exists if $N_a \subset N_l$. Thus, the design of the startup arc, for

a precision entry problem, is not trivial. Certainly, two-body approximations may not be suitable under such circumstances unless extremely close attention is devoted to targeting the precise neighborhood required on the Hill sphere. If the startup arc intersects the Hill sphere, but $N_a \cap N_l = \emptyset$, a targeting process may exhibit a significant reduction in performance, or even difficulties converging on a solution.

One last notable observation is that the dispersions for EEI #1 are all generally centered around the $-180°$ longitude line, as seen from Fig. 3(a). This clearly indicates that all dispersion trajectories intersect the Hill sphere between the Earth and the Moon, closest to the L_1 Earth–Moon libration point region. In contrast, the remaining sites tend to intersect the Hill sphere along the $-\hat{y}$ face, on the L_5 side. In fact, for EEI-2, the dispersion manifolds at the specified entry time extend beyond L_5 before bending towards the Moon and intersecting the Hill sphere. The dispersion manifolds for EEI-6 and EEI-5 come close to L_5 but do extend beyond it for the epoch times selected. This information can be employed, in future studies, in identifying alternate transfer arcs, based on multi-body analysis, that better exploit the dynamical structure of the Earth–Moon system to achieve the specified precision entry goals.

3.1. Startup arcs and converged solutions

As previously mentioned, the nominal return trajectory from low lunar polar orbit is often constructed from conic solutions. In this case, targeting or optimization algorithms are usually required in constructing general baseline transfer trajectories in an n-body regime, for $n > 2$. A multiple-shooting algorithm [21,22], for instance, is one available method that is easily and successfully applied when constructing baseline trajectories. An advantage of multiple-shooting is that it is not a problem specific. The same solution process is applicable in either the CR3BP or in the ephemeris model. A multiple shooting algorithm can be implemented using various strategies including iterations that are potentially multi-step (multi-level). For this application, each iteration involves a single step. To generate solutions in an ephemeris model via multiple shooting, the trajectory is first discretized into a series of patch points—11 in this application. A free variable vector is constructed that contains the 6-dimensional states and epochs associated with all of the patch points. The integration times between patch points

and a slack variable associated with the inequality constraint on total Δv are also included as variables. Maneuvers can be easily inserted or removed at any patch point; continuity in both position and velocity is required at patch points where Δv maneuvers are not implemented. Continuity in time is also enforced at each patch point. The remaining constraints are used to fix the initial state at lunar departure, enforce a desired altitude and flight path angle at Earth arrival, and require that the total Δv be below a desired value. In the current formulation of the problem there are more variables than constraints so a minimum norm solution is used to perform the update. The CR3BP, of course, offers a simplified framework from which to search for transfer arcs that may be better suited to address the complexities of the precision entry problem. In the end, the results must be accurately transitioned and reacquired in the ephemeris model. The process of transitioning solutions between models is generally straightforward with multiple shooting methods [23].

The first step in transitioning a solution between these two systems is to identify the appropriate state transformation. In the ephemeris model, the spacecraft states are typically represented in either Earth centered inertial (ECI) or Moon centered inertial (MCI) coordinates. In the CR3BP, spacecraft states are traditionally expressed in terms of non-dimensional synodic rotating frame coordinates [2]. While the mathematical relation between the ephemeris inertial frame and the synodic rotating frame is easily identified using the available planetary ephemerides, there is one key difference that must be noted. That is, in the CR3BP, the Earth–Moon distance is constant, but that is not the case in the ephemeris model. Subsequently, whenever a solution is transitioned across these two models, it is reacquired using a multiple shooting method to guarantee the resulting states leading to a feasible trajectory.

For instance, consider a baseline three-maneuver lunar return 1.5 km/s solution [1] such as that labeled EPHEM (Nominal) in Fig. 4. This arc represents a converged solution in the ephemeris model, based on an optimized conic initial guess. To demonstrate the flexibility of the numerical algorithm, the ephemeris solution is transitioned to a restricted three-body model – labeled CR3BP (from EPHEM Nominal) – and back to the ephemeris model – labeled EPHEM (from CR3BP). Using the numerically reacquired solution in the CR3BP, the resulting arc and multiple shooting algorithm are employed in a continuation scheme in total Δv that explores other neighboring solutions of successively lower cost. A sample three-burn 1.0 km/s solution, resulting from this approach, is identified both in the CR3BP and in the ephemeris model. These arcs are illustrated in Fig. 5.

Since the second maneuver in this improved 1.0 km/s solution is considerably smaller, further explorations consider a two-maneuver strategy. Eventually, a 0.96 km/s two-burn solution is identified. The 0.96 km/s two-burn solution obtained in the CR3BP ($\Delta V = 1.0$ km/s), and the corresponding trajectory transitioned into the ephemeris model ($\Delta V = 0.96$ km/s), are both depicted in Fig. 6. In this case, the inclination change is accomplished

utilizing Earth–Moon three-body dynamics and the second maneuver at apolune in the original design is no longer required. However, leveraging Earth gravity and eliminating the second maneuver results in an increase in time of flight of up to two days.

Trajectory design in the context of the multi-body problem offers a more diverse solution space, lower energy transfers with correspondingly lower costs, and greater flexibility for global entry targeting. Since lower cost solutions are usually associated with low energy transfers, an increase in time of flight is to be expected. However, a hybrid design approach that incorporates both low-energy segments identified through multi-body analysis and higher energy arcs with shorter flight times can be beneficial in future studies for identifying solutions that exhibit lower cost without a substantial increase in time of flight.

3.2. Entry parameter sensitivities

The numerical evidence collected during the dispersion analysis reveals some useful information regarding the entry constraint coupling and the impact of errors in specific constraints on the targeting process. As previously mentioned, the arrows illustrated in the legend of Fig. 3(a)–(f) indicate the direction of the flow along each dispersion loci. A notable feature present in each and every one of these figures is that the flow evolves in opposite directions for latitude and flight path angle. The sensitivities observed from Fig. 3(a)–(f) and Table 2, along with the flow direction along the loci, suggest a coupling between flight path angle and latitude that may lead to conflicts during the convergence process and, as a result, an increased number of iterations. To explore this further, the present section offers a closer look at entry constraint coupling and its impact on targeter performance.

The next few examples are devoted to characterizing the sensitivity of the targeting process to errors in longitude, latitude, and azimuth when targeting one of these quantities simultaneously along with altitude and flight path angle. The data in Tables 3–5 are associated with two different startup arcs; the three impulse 1.0 km/s solution previously presented, and a three impulse 1.5 km/s solution. Each of these arcs exhibits the desired altitude and flight path angle that was specifically targeted by the multiple shooting process previously discussed. However, the remaining entry parameters were unconstrained at the time. Thus, once the converged solution is identified, the entry state is characterized by a unique unconstrained latitude, longitude, and azimuth. Using these three solutions as startup arcs, Tables 3–5 are compiled in an effort to identify how large the entry error in each of these three parameters can be before the convergence behavior of the targeting process degrades. For the targeting method [1] employed in this study, lack of convergence or an excessively high number of iterations (over 12) before convergence are both considered indicators of degraded performance. In each case, four parameters are always targeted simultaneously; the total cost ($\Delta V < 1.5$ km/s), the altitude (121.912 km), flight path angle ($-5.86°$) and either (a) the longitude, (b) the latitude, or (c) the
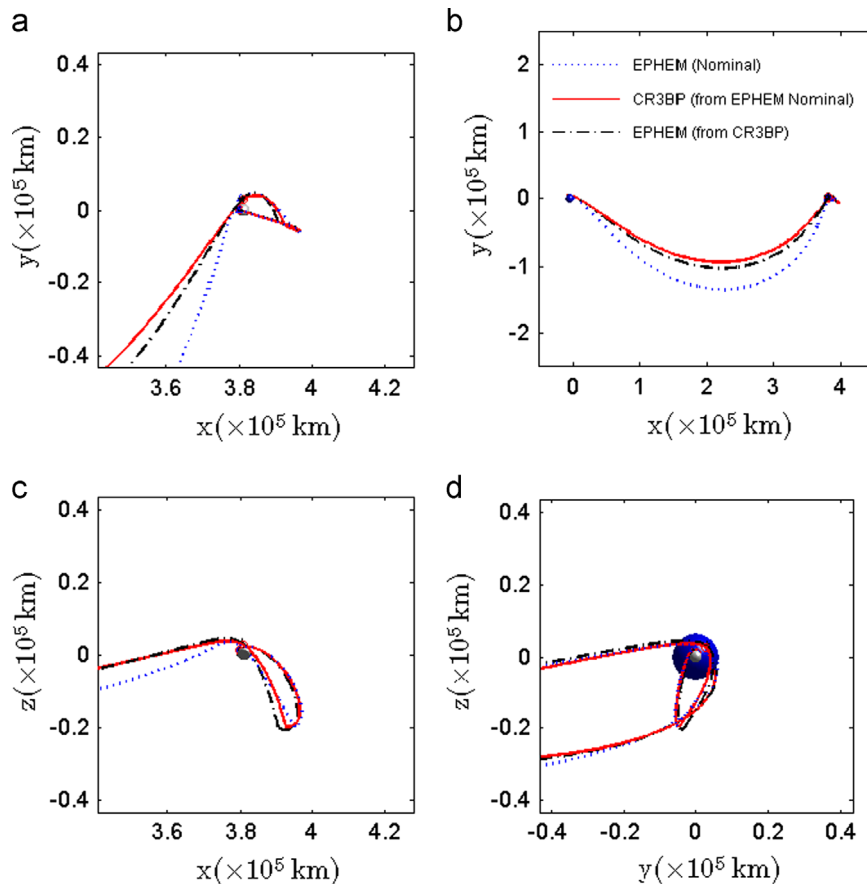
Fig. 4. Three-Burn solution: $\Delta V = 1.5$ km/s.

azimuth. The number listed in the first column of each table represents the error relative to the unconstrained value. Thus, for Solution 1, associated with an unconstrained longitude of roughly $76°$, a $-135°$ error suggests that the target longitude is $-59°$. Since the startup arc is currently at $76°$ longitude, the targeting process has to correct a $-135°$ initial error relative to the startup arc.

3.2.1. Longitude sensitivity

For entry errors in longitude, no convergence threshold is apparent; that is, there is no maximum allowable longitude error at entry beyond which the targeting algorithm [4,1] does not converge. The results in Table 3 suggest that the targeter is able to converge for all cases considered, despite the fact that the entry errors spanned the circumference of the globe. However, some cases do experience performance degradation, particularly cases that employed Solution 1 (i.e. the three-burn 1.0 km/s solution) as inputs. For example, 13 iterations are required to converge the Solution 1 input with an entry longitude error of $-90°$, compared to the 6 iterations required when the entry error is $+90°$. In contrast, only 6 iterations are required to converge the Solution 2 input with entry errors of both $+90°$ $-90°$. This may easily be attributed to the entry timing and the relative location of

the lunar interface state for Solution 1 vs. Solution 2 with respect to the Hill sphere.

To better assess how the quality of the initial guess affects the geometry of the final converged arc, the resulting trajectories may be examined more closely near the Moon. Fig. 7(a)–(f) illustrates a series of Moon centered close-up views corresponding to the $\pm 90°$ entries in Table 3 for Solution 1. The dashed line denotes the initial guess trajectory, and the final trajectory is represented by the solid line. According to Table 3, the $-90°$ perturbation requires 13 iterations to converge while the $+90°$ perturbation only requires 6 iterations. In this case, it is possible that the initial $-90°$ longitude error does not lead to a trajectory that intersects the Hill sphere at all, or does not intersect it in a favorable location relative to the mutual intersection region of the remaining manifolds. Furthermore, an increase in the number of iterations required to converge on a solution corresponds to the increased reshaping of the startup arc to accommodate the constraints. This is particularly evident in the $\pm 90°$ perturbation cases. The xy and xz projections (looking from the Moon towards the Earth) in Fig. 7(d) and (e) show a visibly greater change in geometry as compared to Fig. 7(a) and (b), which is consistent with the higher number of iterations required to converge the $-90°$ error. Because linear targeting algorithms explore the
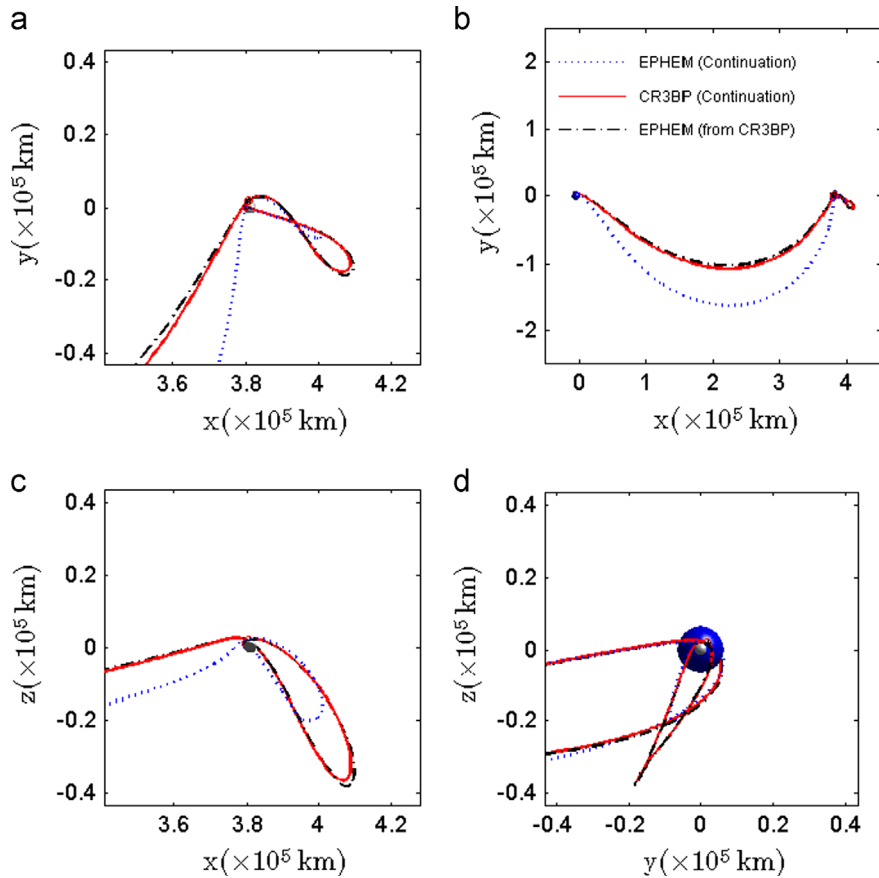
Fig. 5. Three-Burn solution: $\Delta V = 1$ km/s.

neighborhood of the initial guess, the performance of the targeter degrades as the disparity between the startup arc and the final solution increases. Thus, it is important that the initial departure arc selected intersects the same region of the Hill sphere as the dispersion loci shown in Section 3.

3.2.2. Latitude sensitivity

In sharp contrast to the longitude results, the performance of the algorithm exhibits increased sensitivity to errors in latitude. The convergence threshold for latitude errors is less than $2°$. Results for latitude perturbations at entry, shown in Table 4, indicate that even minor errors can have a negative impact on the efficiency of the targeting process. Using Solution 1 (i.e. the three burn 1.0 km/s solution) as a startup arc, just over half the cases are considered converged. Recall that the latitude and flight path angle were previously identified to be the most sensitive parameters according to the Hill sphere dispersion analysis. Furthermore, the flow along the dispersion loci for these two parameters proceeded in opposite directions relative to each other. Thus, it is possible that correcting an error in flight path angle introduces an error in latitude. Then, attempting to correct the resulting error in latitude introduces a greater error in flight path angle. In essence, these two constraints can be at odds with each other during a targeting process, which would explain the

large number of unconverged cases in Table 4 over a seemingly minuscule error in latitude.

As with the longitude results, further insight is gained upon examination of the lunar segments of selected converged trajectories. Fig. 8(a)–(c) illustrates closeup views of the initial and final trajectories for the Solution 2 input with an entry latitude error of $-1.0°$. Fig. 8(d)–(f) and (g)–(i) shows the trajectories for the same input with errors of $-0.5°$ and $+0.5°$, respectively. Again, the dashed lines represent the initial guess trajectories and the solid lines are the final trajectories. Fig. 8(a)–(c) shows the greatest visible geometrical disparity between the initial and converged trajectories, which corresponds to the highest number of iterations required for convergence (23), as compared to the other two cases (11 iterations and 6 iterations, respectively, as shown in Table 4). This is consistent with the trend observed for the longitude example; however, for the latitude case, the Hill sphere dispersions reveal that large trajectory changes near the Moon are required to accommodate small changes at entry interface. Thus, latitude is a dynamically sensitive quantity to target and requires significant changes to the geometry of the departure arc at the Moon.

3.2.3. Flight path azimuth sensitivity

The results of the flight path azimuth sensitivity analysis are given in Table 5. The flight path azimuth
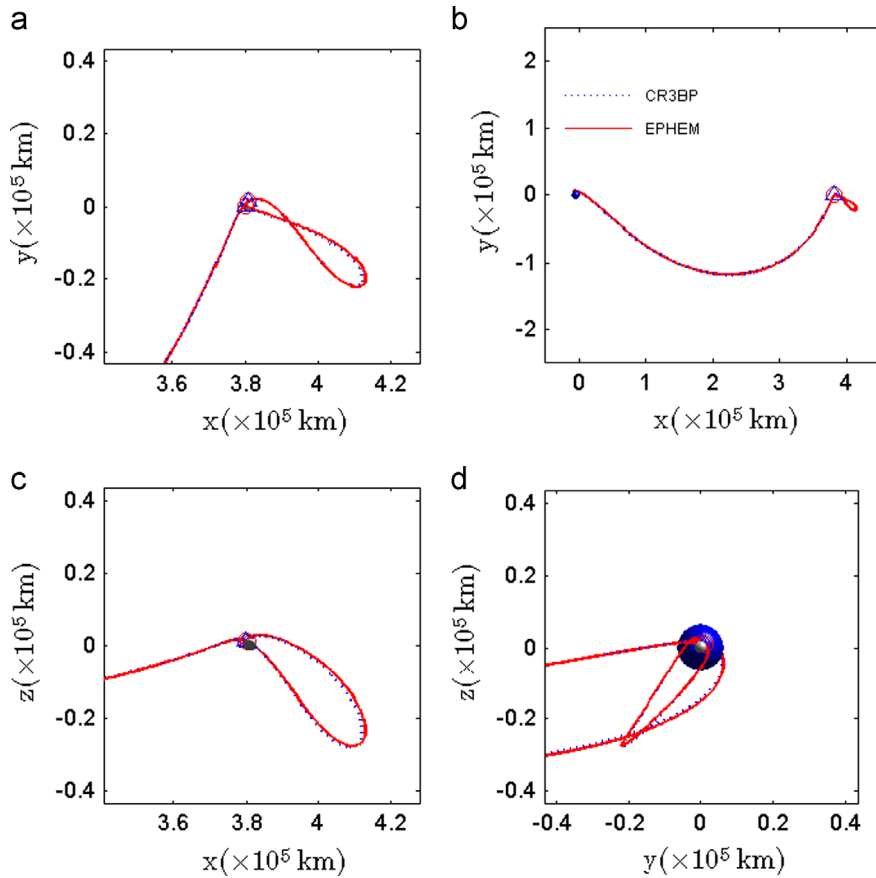
Fig. 6. Two-Burn solution: $\Delta V = 1$ km/s.

Table 3
Example 1: longitude sensitivity.

Longitude Perturbation (deg)	Solution 1 (Unconstr: 76.012189°)		Solution 2 (Unconstr: −138.542302°)	
	Iter.	Total ΔV (km/s)	Iter.	Total ΔV (km/s)
−135	12	1.50	7	1.50
−90	13	1.50	6	1.50
−45	8	1.50	4	1.50
45	8	1.50	5	1.50
90	6	1.50	6	1.50
135	6	1.50	7	1.50
180	10	1.50	10	1.50

Table 4
Example 2: latitude sensitivity.

Latitude Perturbation (deg)	Solution 1 (Unconstr: 3.594905°)		Solution 2 (Unconstr: −1.906029°)	
	Iter.	Total ΔV (km/s)	Iter.	Total ΔV (km/s)
−1.5	–	DNC	–	DNC
−1.0	21	DNC	23	1.50
−0.5	8	1.50	11	1.50
−0.25	4	1.44	6	1.50
0.25	4	1.50	4	1.50
0.5	–	DNC	6	1.50
1.0	44	1.50	13	1.50
1.5	–	DNC	17	1.50

DNC=Did not converge.

locus on the Hill sphere was narrower than the rest, indicating that small changes in the departure geometry at the Moon are required to accommodate changes in flight path azimuth at entry, that is, as long as the other quantities targeted are not in conflict. In each of the cases presented here, and in the previous sections, the altitude and flight path angle are always targeted as well. Thus, if the flight path azimuth targeted is in conflict with the flight path angle specified, that too will degrade the performance of the targeting algorithm. Although the azimuth results presented here show noticeably improved convergence over the latitude sensitivity

results, the convergence threshold, or the entry error range beyond which the targeter cannot converge, for this case is still only $\pm 36°$. The Hill sphere analysis did reveal that the azimuth dispersions exhibit a certain degree of inertia. That is, small changes at Earth entry do not correspond to such wide dispersions at the Hill sphere as other parameters examined in Section 3 do. Referring back to Fig. 3, the range of azimuth dispersions is typically no more than approximately 30°, while other parameters such as latitude and longitude can span 90° or more. However, it is also true that the azimuth and flight

path angle loci flow in directions that are almost normal to each other. Thus, once the solution sought leaves the vicinity of the intersection of these two loci, it may place the targeter in a neighborhood of phase space that does not include the desired solutions. Thus, the targeting process has to work harder and longer to escape that neighborhood in search for one that offers more auspicious transfers.

To verify these observations, consider the Moon centered close-up views presented here. Fig. 9 shows the initial and final Solution 2 trajectories near the Moon for azimuth errors of −24°, in Fig. 9(a)–(c). Similar images are presented for the +24° error in Fig. 9(d)–(f). The −24° case requires a total of 31 iterations to converge, while

Table 5
Azimuth sensitivity.

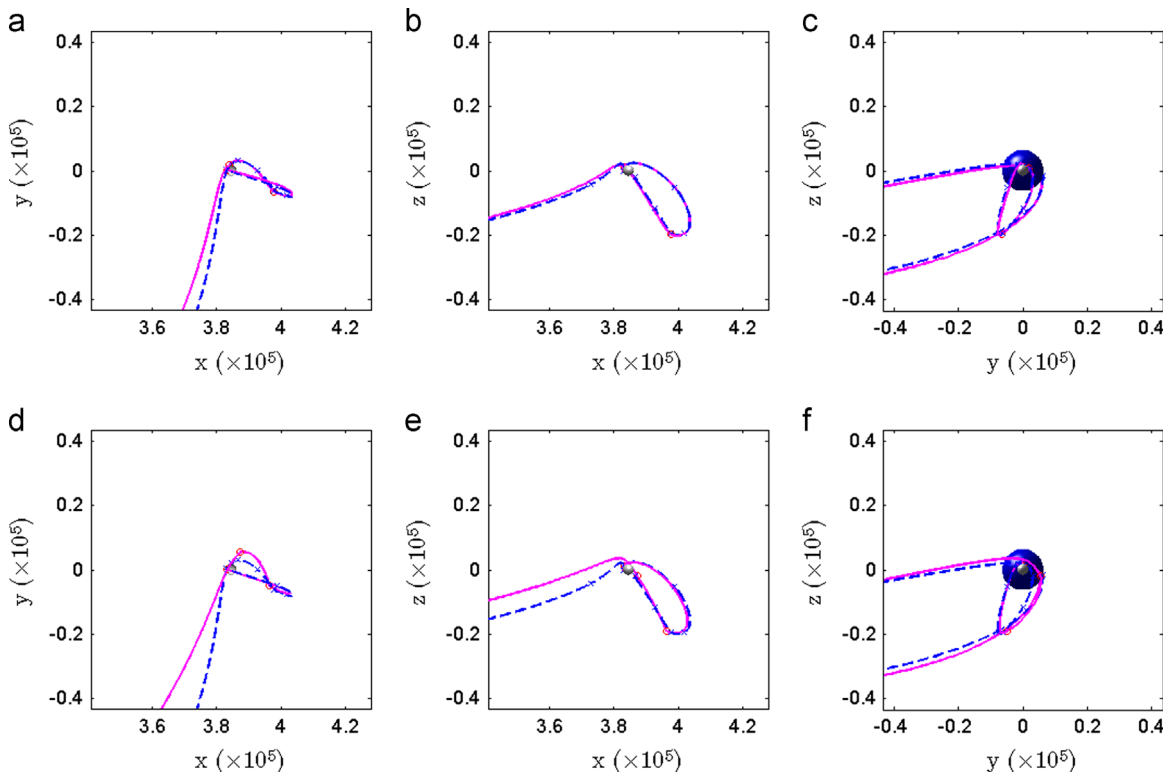| Azimuth Perturbation (deg)	Solution 1 (Unconstr: 8.985265°)		Solution 2 (Unconstr: 4.172730°)	
	Iter.	Total ΔV (km/s)	Iter.	Total ΔV (km/s)
−36	30	1.50	30	1.50
−24	31	1.50	31	1.50
−12	33	1.50	30	1.50
−6	4	1.16	–	DNC
6	4	1.36	4	1.36
12	10	1.50	5	1.26
24	11	1.50	6	1.50
36	15	1.50	14	1.50

DNC=Did not converge.

the +24° case converges in only 11. In both the cases, the lunar departure geometry is not significantly affected. What is affected, however, is the arrival geometry, best visualized from the yz-plane projections. Curiously, the case that required the least number of iterations to converge is the one that exhibits the most significant changes in arrival geometry. While this may seem counter-intuitive at first, it is actually not surprising. The fact that the overall geometry of the −24° case did not change significantly in 31 iterations suggests a great degree of resistance to small changes. Since the targeting algorithm entails a linear corrections process, one that employs a minimum norm solution, the corrections implemented are the smallest possible changes that lead to a feasible solution. The behavior exhibited by this particular solution can be explained in the context of relative stability.

Consider, for instance, the L_1 collinear libration point vs. the L_5 collinear point. The collinear points are all unstable [2]. Thus, small perturbations are promptly amplified as time flows forward. In contrast, the equilateral point L_5 is marginally stable, at least in the linear system. In the ephemeris model, these points do not actually exist. However, the region near the instantaneous libration points exhibits a similar degree of relative stability. Perturbations near the collinear points are quickly amplified, while perturbations near the triangular point grow at a slower rate. It is not surprising, then, to find that there are regions of phase space where solutions are less susceptible to perturbations than others.
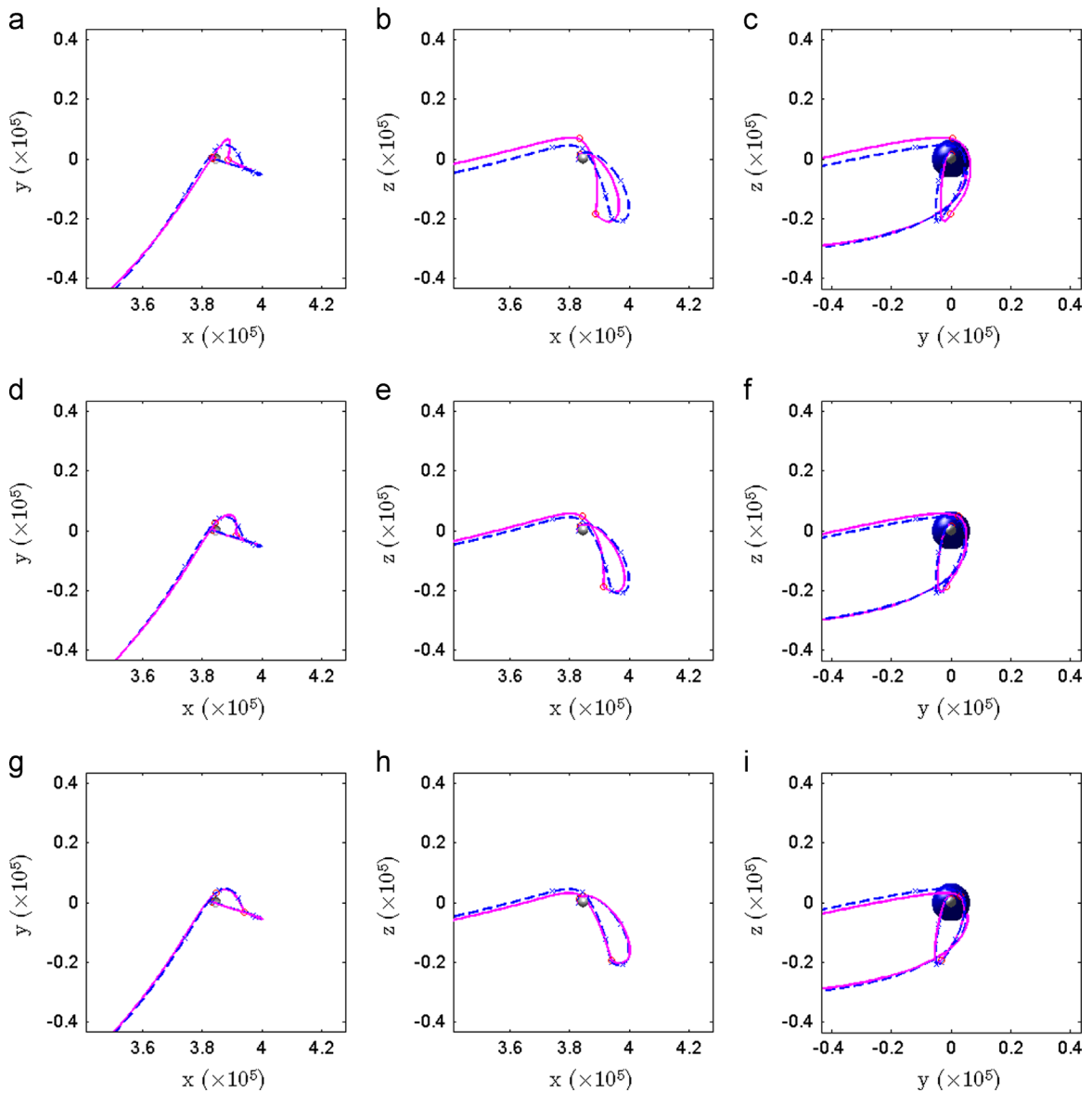

Fig. 7. Solution 1: impact of longitude error on lunar departure geometry. (a) +90°. (b) +90°. (c) +90°. (d) −90°. (e) −90°. (f) −90°.

Fig. 8. Solution 2: impact of latitude error on lunar departure geometry. (a) $-1°$. (b) $-1°$. (c) $-1°$. (d) $-0.5°$. (e) $-0.5°$. (f) $-0.5°$. (g) $+0.5°$. (h) $+0.5°$. (i) $+0.5°$.

It was previously noted that the EEI-2 dispersion manifolds extended beyond and around L_5 before intersecting the Hill sphere. Furthermore, the manifolds for EEI-5 and EEI-6 passed interior but very close to L_5 as well. Upon close inspection, a trend is quickly observed. For the entry parameters selected, the azimuth loci on the Hill sphere are narrower in length, and closer to the zero-latitude plane, than any other loci for the cases when the manifolds extended close to L_5 (EEI-2, EEI-5, and EEI-6). Although almost all the dispersion manifolds for EEI-2, EEI-5, and EEI-6 passed near or around L_5, only the azimuth – which affects the Earth arrival plane – was significantly affected by this. The flight path angle loci, for instance, span a very large latitude range on the Hill sphere for all EEI states considered. The key, it seems, is in

the fact that both flight path angle and azimuth are targeted at the same time. One constraint, namely flight path angle, is very sensitive to small changes while the other is not. Thus, the targeting algorithm is susceptible to the inertia induced by the azimuth constraint, in this case. Convergence ensues, but at a much slower rate as a result.

4. Conclusions

The present study considers the dynamical aspects of precision entry transfers in the perturbed restricted three-body problem. In particular, the interaction between the entry dispersion manifolds and the Hill sphere are studied to assess entry constraint coupling and sensitivities, as well as their impact on the design of feasible startup
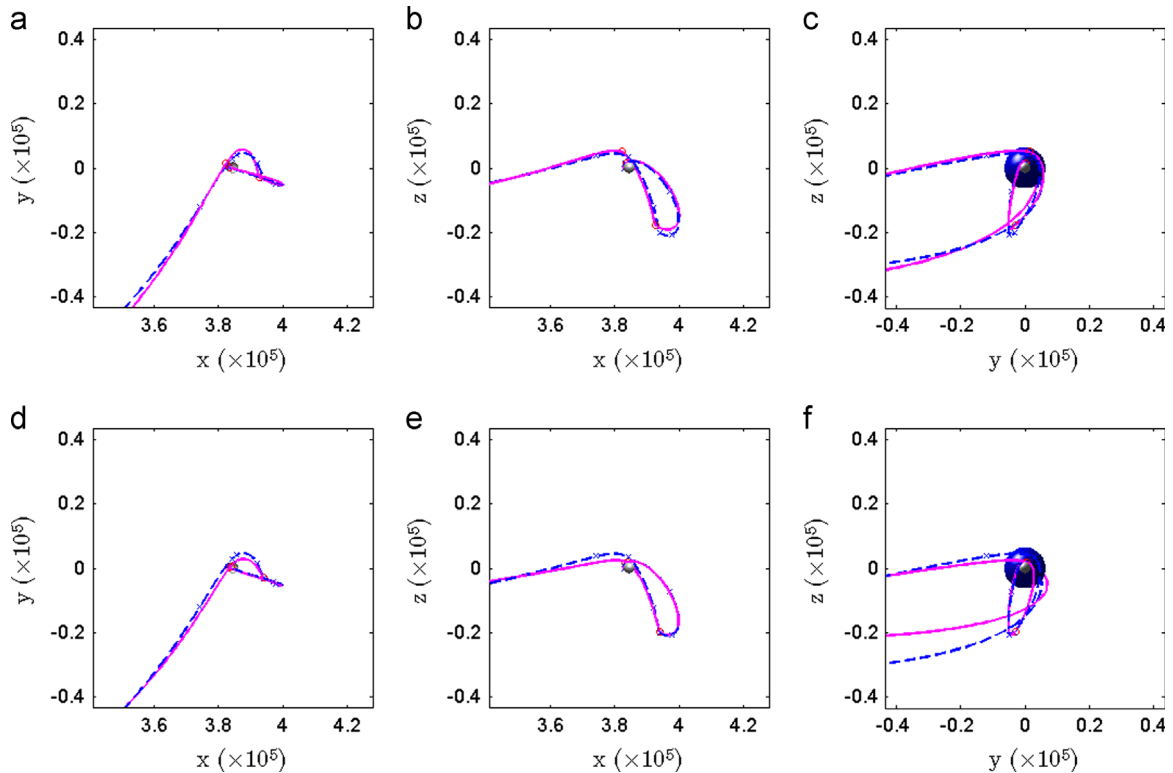
Fig. 9. Solution 2: impact of Azimuth error on Lunar departure geometry. (a) $-24°$. (b) $-24°$. (c) $-24°$. (d) $+24°$. (e) $+24°$. (f) $+24°$.

transfer arcs. An initial investigation into the use of third-body effects to reduce the fuel cost is also presented. The application of dispersion manifold analysis is demonstrated through an example involving the Orion trans-Earth injection sequence. A measurable degree of coupling is identified between flight path angle and both azimuth and latitude, though each of a different kind. When targeting multiple entry constraints it is observed that the azimuth constraint introduces a measurable degree of inertia to small perturbations, while the latitude constraint contributes an increased sensitivity to small errors.

Acknowledgments

References

[1] B.G. Marchand, M.W. Weeks, C.W. Smith, S.K. Scarritt, Onboard autonomous targeting for the trans-Earth phase of Orion, J. Guidance Control Dyn. 33 (3) (2010) 943–956. also available as AIAA Paper no. 2008-7262.

[2] V. Szebehely, Theory of Orbits: The Restricted Problem of Three Bodies, Academic Press, New York, 1967.

[3] D.P. Hamilton, J.A. Burns, Orbital stability zones about asteroids, Icarus 92 (1) (1991) 118–131.

[4] B.G. Marchand, K.C. Howell, R.S. Wilson, Improved corrections process for constrained trajectory design in the n-Body problem, J. Spacecraft Rockets 44 (4) (2007) 884–897.

[5] S.K. Scarritt, B.G. Marchand, M.W. Weeks, An autonomous onboard targeting algorithm using finite thrust maneuvers, in: AIAA Guidance, Navigation, and Control Conference and Exhibit, Chicago, IL, 2009, aIAA 2009-6104.

[6] A.E. Bryson, Y.-C. Ho, Applied Optimal Control: Optimization, Estimation, and Control, Taylor & Francis, New York, 1975.

[7] D.G. Hull, Optimal Control Theory for Applications, Springer-Verlag, New York, 2003.

[8] J.T. Betts, Survey of numerical methods for trajectory optimization, J. Guidance Control Dyn. 21 (2) (1998) 193–207.

[9] J. Betts, Practical Methods for Optimal Control Using Nonlinear Quadratic Programming, Society of Industrial and Applied Mathematics, Philadelphia, PA, 2001.

[10] J. Betts, S. Erb, Optimal low thrust trajectories to the moon, SIAM J. Appl. Dyn. Syst. 2 (2) (2003) 144–170.

[11] J. Betts, Very low thrust trajectory optimization using a direct sqp method, J. Computat. Appl. Math. 120 (1–2) (2000) 27–40.

[12] M. Lo, et al., Genesis mission design, J. Astro. Sci. 49 (1) (2001) 169–184.

[13] B.T. Barden, K.C. Howell, Fundamental motions near collinear libration points and their transitions, J. Astro. Sci. 46 (4) (1998) 361–378.

[14] D. Grebow, M. Ozimek, K. Howell, D. Folta, Multi-body orbit architectures for lunar south pole coverage, J. Spacecraft Rockets 45 (2) (2008) 344–358.

[15] E. Standish, Jpl planetary and lunar ephemerides, de405/le405, Tech. rep., The Jet Propulsion Laboratory, iOM 312.F98048.

[16] C.A. Ocampo, R.R. Saudemont, Initial trajectory model for a multi-maneuver Moon to Earth abort sequence, in: AAS/AIAA Space Flight Mechanics Meeting, Savannah, GA, 2009, Paper no. AAS 09-195.

[17] N.X. Vinh, A. Busemann, R.D. Culp, Hypersonic and Planetary Flight Mechanics, University of Michigan Press, Ann Arbor, MI, 1980.

[18] J.C. Harpold, J.C.A. Graves, Shuttle entry guidance, J. Astron. Sci. 27 (1979) 239–268.

[19] W.H.T. Loh, Re-Entry and Planetary Entry Physics and Technology, University of Michigan Press, Ann Arbor, MI, 1980.

[20] P.A. Penzo, An analysis of Moon-to-Earth trajectories, Technical Report NASA-CR-132100, Space Technology Laboratories, Inc., Redondo Beach, CA, October 1961.

[21] H.B. Keller, Numerical Solution of Two Point Boundary Value Problems, CBMS-NSF Regional Conference Series in Applied Mathematics, vol. 24, Society for Industrial Mathematics, 1976.

[22] G. Gómez, J. Masdemont, C. Simó, Quasihalo orbits associated with libration points, J. Astron. Sci. 46 (2) (1998) 135–176.

[23] T. Pavlak, K. Howell, Evolution of the out-of-plane amplitude for quasi-periodic trajectories in the Earth–Moon system, in: IAF 62nd International Astronautical Congress, Cape Town, South Africa, 2011.